






Patch-size Segmentation of Small-Scaled Magnetic Resonance Images of the Prostate with Prior Information

Heng Zhang ¹ , Atul Thakur ²  and Xiangzhi Wei³ 

¹ Shanghai Jiao Tong University, hunter_zhang@sjtu.edu.cn

² Indian Institute of Technology Patna, athakur@iitp.ac.in

³ Shanghai Jiao Tong University, antonwei@sjtu.edu.cn

Corresponding author: Xiangzhi Wei, antonwei@sjtu.edu.cn

Abstract. Efficiently reconstructing the Prostate tissue from a sequence of magnetic resonance images is a critical job for fast male health examination in highly populated hospitals, which requires a fast examination with acceptable accuracy. Existing methods rely on rather heavy data-training processes or slow interactive manual selection to obtain an accurate segmentation result. In this paper, a trade-off between accuracy and efficiency is achieved by manually choosing a coarse region of interest that contains a target feature on the first image, and iteratively segmenting the current magnetic resonance image by detecting only the neighboring zones of the projection of the computed contour from the previous image, which avoids the computation in the vast useless regions of the images. The feature contour segments are acquired in a patch-by-patch manner where a patch corresponds to a sliding window. We performed validation experiments on PROMISE 12 data set, which reveals that our approach can lead to a Dice Similarity Coefficient of $89.21 \pm 1.82\%$ and Relative Volume Difference of $-10.44 \pm 6.46\%$ computed in an average time of 3 seconds plus an average preprocessing time of 10 seconds.

Keywords: prostate segmentation, Canny operator, prior information.

DOI: <https://doi.org/10.14733/cadaps.2022.38-53>

1 INTRODUCTION

Prostate cancer incidence is ranked second in all men's cancer incidence rate all over the world [1] and prostatic hyperplasia is also a common disease of the elderly men. The diagnosis of prostate disease is carried out by using computed tomography (CT), biopsies guided by transrectal ultrasound (TRUS), and magnetic resonance imaging (MRI) [2]. MRI has gradually replaced TRUS and CT as the preferred clinical examination method due to its excellent performance in soft tissue imaging. The MRI images need to be visually inspected, and thus the examination results get influenced by the radiologist's experience; and this process is often time-consuming. Considering these, researchers have proposed many automatic or semi-automatic segmentation methods to overcome the difficulties caused by noise, non-uniform gray level, low contrast, and intensity

inhomogeneity. These segmentation algorithms of MR images are mainly classified into three categories: atlas-based segmentation, deep-learning based segmentation and model-based segmentation. In the following, we shall review the works closely related to the three categories mentioned above.

The atlas-based segmentation selects a set of training images, then annotate their contours manually as labels [3-9]. The training images and corresponding contour labels called *atlas* and *labelled atlas*, are fused by *non-rigid registration* (NRR) to create reference images for segmenting new images [3]. In the process of non-rigid registration, the anatomical marks (special points or faces) of the atlas are parameterized and aligned with the corresponding parts of the target image to guide the deformation of the rest part of the target image. The corresponding labelled atlas indicates whether a voxel is part of the prostate or not [4]. The operation of label fusion can be done in many ways. For example, gray level averaging, majority voting (VOTE), simultaneous truth and performance level estimation (STAPLE) [5] and selective and iterative method for performance level estimation (SIMPLE) [6]. Many researchers have developed various methods based on the atlas-based segmentation. For example, Klein et al [7] proposed an automatic atlas-based segmentation method that applied non-rigid registration to prostate MR image and binary atlas image, and then selected the best matched atlas image to segment medical image; Chandra et al [4] proposed an atlas-based deformable model, in which the image feature model was used to deform the initialized surface by template matching image features via normalized cross-correlation to the features of the scan; Yang et al [8] proposed a prostate segmentation method based on 3D multi-atlas MR images. The above methods are suitable for training and learning medical images with sufficient image data, but the training needs the support of annotated image labels, which is often time-consuming.

Many scholars combined traditional techniques with deep-learning methods to conduct image segmentation, which has been made possible due to the availability of a large quantity of annotated medical image data on the network [10-21]. Many net frameworks like *Image-net* [10], *Alex net* [11], *VGG-net* [12], *Google net* [13], *U-Net* [14], *V-net* [15], *Fast R-CNN* [16], *DCAN* [17], and *GAN* [18] can also be used for medical image segmentation. Zhu et al [19] proposed a convolution neural network with deep supervision, which can detect the fuzzy boundary of prostate tissue. Isensee et al [20] proposed a framework called *no-new-Net* (nnU-Net), which could be automatically adapted to any given medical subdivision data set without the need of manual adjustment of the parameters. Cheng et al [21] proposed a method of combining atlas-based *active appearance model* with deep learning model that initialized prostate contour with fewer atlas and improved the segmentation result with deep learning CNN model. These methods used deep-learning to achieve good results in segmentation. But they rely on a large scale of annotated data for training the network and complicated parameter adjustment to avoid over-fitting.

Active Contour Model (ACM) is a popular model-based image segmentation method without using annotated image data. In medical image segmentation, ACM was first introduced by Kass et al [22]. It can provide a closed and smooth contour or surface of the target object and be applied to various 2D and 3D segmentation scenes [23]. According to the information used in the energy function, ACM can be roughly classified into edge-based model [24,25] and region-based model [26-29].

ACM can be incorporated with other techniques to improve its performance. For example, Yang proposed an efficient ACM with a new energy function using the globally convex segmentation method that included the edge information into the energy functional [30]. Wang proposed an ACM for image segmentation and bias correction, which considered both the spatial information and the local image contents [31]. The ACM with the prior information is one of the promising approaches in addressing this problem, where the prior information includes the location of interesting region, size and shape of object [32-41]. There are many similar approaches that utilize the prior information to segment the medical images. Yan et al [37] proposed a *partial active shape model* (PASM), which used some parts of the prostate contour with salient boundary features for shape estimation. Vikal et al [38] proposed a semi-automatic algorithm in which the

contour of prostate MR image slice is used as the prior information to estimate the adjacent slices. Andrade et al [39] used the prior knowledge of prostate shape to guide the evolution of initial contour, and used the energy function to segment the image. Yang et al [40] proposed a hierarchical prostate segmentation formulation via *level set* clustering with the prior shape information that used the medium image slice's location to reduce the impact of the background and guide the segmentation of other slices. Jia et al [41] used the prior information of prostate MR as the reference of image coarse segmentation, and then used the depth neural network to refine the image segmentation to obtain more accurate results.

Inspired by the methods based on prior information, this work proposes an efficient method that uses the shape and brightness of the prostate as prior information to guide the subsequent image segmentation wherein the information of the brightness is inherently used in the boundary calculation of the Canny operator [42].

The main contributions of this paper: Given a sequence of prostate MR images, we propose an interactive method to locate the rough contour of the prostate tissue of the first MR image in a fast manner (selected manually); after that, iteratively, the contour in the next MR image is obtained by investigating a narrow zone containing the projection of the current contour, which avoids the search among the vast useless regions and speeds up the computation efficiency.

The remainder of the paper has been organized as follows: Section 2 presents the details of the developed approach; Section 3 presents the results of a set of validation experiments; Section 4 concludes the paper with some discussions.

2 OUR PROPOSED METHOD

A fast medical image segmentation method based on the prior information of the target image is proposed in this paper. The prior information of medical image is the experience and knowledge obtained from professional radiologists and related studies, including the image constraint information, the location of the region of interest (ROI), and the object's size or shape.

In the following, Section 2.1 presents the prior information; Section 2.2 presents the crucial steps of reconstructing the 3D prostate model from a sequence of MR images; Section 2.3 presents our patch-size segmentation algorithm for a single image.

2.1 The Prior Information

As an important gland of the male body, the dimension of prostate is generally no more than 40mm × 30mm × 30mm [43]. According to the anatomical characteristics of the prostate, the contour of the prostate is gradually changed in the same sequence of MR images since the sampling interval is typically less than 1 mm. This property can be used as shape constraint information of the target. The contour obtained in the current image can provide shape constraint information for the next image. In addition, the prostate, the adjacent bladder, the muscle, and other tissue components have different brightness in MR images. These properties can be used as the prior information for image segmentation, which is presented in the following section.

2.2 An Efficient Image Segmentation Algorithm

Given a sequence of MR images, the core idea of the algorithm proposed in this paper is using the prior information of the prostate contour as the shape constraint to guide the search of the contour of the prostate in the next image. Typically, a prostate is smooth, and the change between two thin slices is small. Therefore, we can use the known contour to limit the ROI of the images to be segmented. In this way, we can avoid the search in the useless regions and reduce the computation cost, thus achieving the purpose of fast image segmentation. Since there is no accurate contour information for reference for the vague MR images, we can manually mark a rough region that contains the prostate on the first MR image and use it as reference to segment subsequent images. Note that many prostate MR images are vague such that any algorithm may

not be able to correctly identify a precise contour of the prostate than our human eyes. For example, in Figure 1(a), it is reasonably hard for any computer algorithm to identify the exact zone of the prostate (Figure 1(b)), which requires a lot of effort of training and parameter optimization. However, as shown in Figure 1 (c), our human eyes can intuitively identify the prostate, and therefore we can draw a zone of the prostate efficiently (but slightly different from the ground truth). Thus, the manually identified prostate contour on the first image is taken as the prior information to identify the prostate contours on the next MR images iteratively.

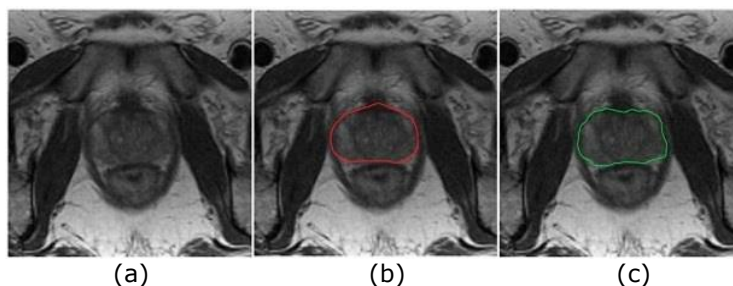


Figure 1: The prostate MR image: (a) the original image, (b) the ground truth of prostate marked with a red curve, and (c) the manual selection of ROI (green curve).

At the beginning, we load a sequence of prostate MR images of a patient, where the sequence corresponds to a range of male-body that contains the prostate tissue (scanning other parts of the body is meaningless); and then choose the middle image of the sequence, which contains a contour of the prostate. The major steps for constructing the 3D model of the prostate are as follows:

- Mark a rough ROI of a middle image manually.
- Segment the image into ROI and background.
- Compute the feature contour in the ROI take it as the reference, and invoke Algorithm 2 in Section 2.3 to obtain the accurate contour of the prostate in an adjacent image.
- Repeat the previous step until no new contour is detected.
- Reconstruct the 3D prostate model based on the set of contours.

In the following, Figure 2 and Algorithm 1 presents these steps in details.

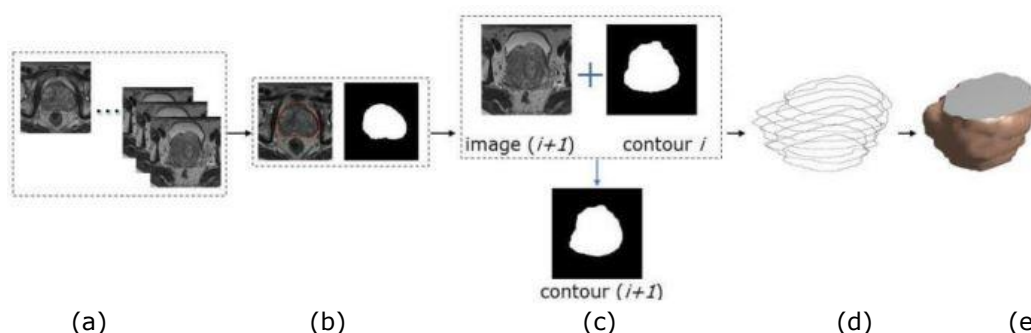


Figure 2: The major steps of our proposed algorithm: (a) Input the MRI image sequence, (b) Mark the rough ROI of first image manually, (c) Segment precise contour of each image of the prostate using Algorithm 2 in Section 2.3, (d) Obtain a sequence of precise contours, (e) Reconstruct the 3D model based on the segmentation.

Algorithm 1 Reconstruct_Prostate(M)

Input: A sequence of MR images M ;

Output: The 3D model of prostate reconstructed;

1. M_i := the first image containing the target tissue;

2. mark the approximate ROI of M_i manually;

3. $C := \emptyset$;

4. C_i := the target contour in set M_i ;

5. $j = i$;

6. **while** ($i \neq -1$ or $j \neq |M|$) **do**

// process the while loop if any forward or backward adjacent image exists in the set

if Compute_Current_Feature_Contour(C_i, M_{i-1}) \neq NULL **then**

// keep computing the feature contour of the previous image in sequence

C_{i-1} := Compute_Current_Feature_Contour(C_i, M_{i-1});

$i := i - 1$;

if Compute_Current_Feature_Contour(C_i, M_{j+1}) \neq NULL **then**

// keep computing the feature contour of the next image in sequence

C_{j+1} := Compute_Current_Feature_Contour(C_i, M_{j+1}); *//forward computation*

$j := j + 1$;

7. $C := C \cup \{C_i\}$;

8. Reconstruct the 3D model of prostate based on C ;

2.3 Our Proposed Segmentation Algorithm

In this section, we shall elaborate on using the shape constraint information of the segmented object (of the previous image) to calculate the contour of the prostate tissue in the current image.

The manually selected contour includes the ROI that contains the target contour and is very helpful in local image segmentation (around the target object), which merely uses local image information rather than global image information. In processing each image, we select a sequence of reference points (sampling over the contour by an interval of 5) along the already computed contour (in the previous image) to locate the sliding window for our local image segmentation in the current image. Since the shape of a nut liked organic object is changed gradually, we can choose an appropriate dimension to ensure that the real boundary of the target feature is included in the sliding window.

Many edge detection algorithms have been proposed based on gradient and Laplacian derivatives, which are critical in image processing. The edge detection algorithm based on the traditional method is calculated by detecting the maximum value of the first derivative or the zero crossing of the second derivative. Although the first-order differential operators such as Roberts operator, Prewitt operator and Sobel operator have many advantages in simple calculation and fast implementation, they are more sensitive to noise [44-47]. The second order differential operators (including Laplace operator, LOG operator and Canny operator) have better robust performances to noise by filtering the image before the edge detection. All these algorithms are not designed to identify high frequency impulse noise [48]. In practical applications, medical images contain the boundaries, shadows and noises of objects, so these algorithms are difficult to distinguish the original edges from noises or trivial geometric figures. For this reason, we have carried out medical image segmentation experiments on different operators. The experimental results are available in the Appendix at the end of the paper, and Canny operator is finally chosen.

The first step of the traditional Canny algorithm is to smooth image. Canny algorithm deduced the first derivative of Gaussian function, which is the best approximation of the optimal edge detection operator. The second step is to use limited difference of 2*2 neighboring area to calculate the value and direction of image gradient [49]. And then the Canny algorithm performed non-maximum suppression (NMS) to locate the edge points each of one-pixel width. Finally, the double-threshold method is used to select edge points [50].

In our case, each MRI images is of size 128*128. In order to narrow the search range, meantime to ensure that the Canny operator can effectively calculate the image gradient, the size of the sliding window used in the proposed algorithm should be larger than the neighboring area of Canny operator, but no more than a quarter of the original image. Through a trial-and-error process by testing the sliding window of size 5*5, 7*7, 9*9, 11*11 and 13*13, it is found that 11*11 is a reasonable choice for the images with nice accuracy and efficiency.

We use the Canny operator to obtain the contour information in this window. By moving the sliding window continuously along the reference contour, the entire contour of the target feature can be obtained by stitching the contour segments together. Formally, given the reference contour C_i of the former image and the current image M_{i+1} , our algorithm of computing C_{i+1} for M_{i+1} is presented as follows. Note that the forward computation of C_{i-1} for M_{i-1} can be done similarly.

Algorithm 2 Patch_Size_Segmentation (C_i, M_{i+1})

Input: The reference contour of former image C_i and the current image M_{i+1} ;

Output: C_{i+1} ;

1. $C_{i+1} := \emptyset$;
 2. $P :=$ all boundary points of the reference contours;
 3. **for** each point p_i for every interval of k points along C_i **do**
 set p_i as the center of the sliding window;
 $I_i :=$ the sub-image covered by the sliding window centered at p_i ;
 $S_i :=$ the feture contour in I_i by invoking the Canny operator;
 $C_{i+1} := C_{i+1} \cup \{S_i\}$;
 4. **return** C_{i+1} ;
-

Figure 3 shows the contour segmentation process. The first row of Figure 3 presents the process of computing the boundary of the prostate tissue in the same MR image, where the rightmost rectangular box in each image indicates the current position of the sliding window. The second row of Figure 3 presents the sub-images extracted by the sliding window at the corresponding moment, and the third row presents the results of image segmentation of each sub-image. A portion of the boundary obtained from the previous image is enclosed in a rectangular box in each image. The small rectangle in each image of the third row indicates the portion of contour obtained from the previous window, which is also the common contour part of the two consecutive contour portions of a pair of adjacent windows.

3 EXPERIMENT

In this section, we present the validation of the developed algorithms by conducting prostate MR image segmentation on a data set. Section 3.1 presents the data set and our evaluation method, and Section 3.2 shows the segmentation results, Section 3.3 shows our 3D reconstruction results, and finally, Section 3.4 shows our comparison with existing typical results.

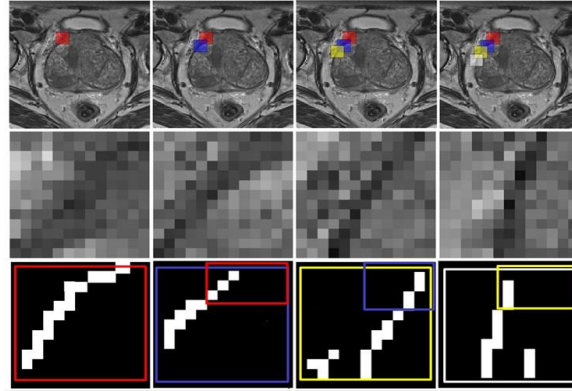


Figure 3: Identifying an accurate contour. Colored windows indicate the sliding window's positions. In the third row, large rectangle boxes represent the results obtained by using edge detection in each iteration, while the small rectangle box shows the overlap between two iterations.

3.1 Data Set and Evaluation Method

To demonstrate the proposed algorithm's performance, we conducted our experiments on Prostate MR Image Segmentation 2012 (PROMISE12) data set [51].

The data set of PROMISE 12 has 50 training-sets and 30 test sets (and each set contains 32 images). The dataset is transversal T2-weighted and from multi-centers. In general, the pixel intensities and the appearance characteristics of prostate MR images may be greatly different due to signal-to-noise ratio, bias, and instrument resolution [51]. The resolution of the images is 128×128 pixels, and the image intensities of different groups may also have significant variations. For validation, we randomly selected 10 data sets from PROMISE 12 that contains the ground truth to demonstrate the performance of our proposed algorithm.

Our algorithm has five main parameters: Δs represents the step length (in terms of pixels), which is the moving distance of the sliding window from one sub-image to the next, n represents the sub-image dimension, σ represents the Gaussian filter coefficient, the built-in parameter of image denoising before image segmentation, ε represents the ratio of non-edge pixels in each sub-image, and τ represents the stimulus value that Canny operator recognizes as pixel boundary. During the process of the experiment, the main parameters of image segmentation are set by default as follows: $\Delta s = 2$, $n = 11 \times 11$, $\sigma = 1.4$, $\varepsilon = 0.9$, and $\tau = 0.45$.

To measure image segmentation accuracy, we use Dice Similarity Coefficient (DSC) [52] and Relative Volume Difference (RVD) [53]. DSC is one of the most commonly used overlap-based indicators. It is mainly used to measure the proportion of the same pixels between the segmentation result and the ground truth, where higher values represent more accurate segmentation results. RVD is also an important indicator used to measure whether the segmentation result is over-segmentation or insufficient segmentation than the ground truth value. DSC and RVD are defined as follows.

$$\text{DSC}(X, Y) = \frac{2|X \cap Y|}{|X| + |Y|} \quad (3.1)$$

$$\text{RVD}(X, Y) = \left(\frac{|Y|}{|X|} - 1 \right) \times 100\% \quad (3.2)$$

Where $|X|$ is the number of non-zero pixels of the set X , and X is the segmentation results of proposed algorithm, and Y is the ground truth provided by the datasets. The value of DSC ranges from 0 to 1, and the higher the value of DSC is, the more accurate the result of the algorithm is. The value of RVD is the percentage of the difference between the obtained volume X , and the ground truth volume Y . A positive RVD value indicates under-segmentation of the prostate. In contrast, a negative RVD value indicates over-segmentation.

3.2 Segmentation of the PROMISE 12 Data Set

We have implemented our algorithm in C++ with OpenGL API on a laptop with 8 GB RAM. The segmentation results of 10 randomly selected data sets from PROMISE 12 are shown in Figure 4, Table 1 and Table 2. In Figure 4, the first row shows the original medical images whose prostate components are marked with red curves according to the ground truth provided by the PROMISE 12. The second row shows our segmentation results. The white shadow parts are the segmentation results of our proposed algorithm, and the ground truth are marked with red curves for comparison. The third row shows the results of overlapping the segmentation results with the original images. As shown in the second row, the segmentation results of our proposed algorithm for prostate MR images are almost the same as the ground truth. Although the results are reasonable, our segmentation results are over-segmented slightly, i.e., the contour obtained is larger than the real value. The over-segmentation can be attributed to the choice of segmentation parameters, especially the dimension of sub-images (or sliding windows). In our example, the size of each sub-image is set to 11×11 ; in general, this can be determined through a set of simple segmentation experiments on a small sample of images.

Among the five parameters related to our algorithm, we find that the change of sub-image size, the percentage that pixels do not belong to edges, and the threshold rate has a more critical impact on the segmentation results. In contrast, the pixel moving step and Gaussian filter coefficient changes have subtle influence on the segmentation result. Although a larger pixel moving step can reduce the amount of calculation in the segmentation process, the segmentation result may be discontinuous or unstable if it is too large. Due to segmentation errors, the pixels that were determined as boundary edges earlier may be mistakenly treated as non-edge in the subsequent calculations. Therefore, for the pixel moving step-size, 5 was found to be a reasonable choice in our case after a simple experiment. Usually, Gaussian filter parameters are used to filter the image noise in the process of image preprocessing. Our algorithm can weaken the impact of noise by only focusing on a small local region of interest. Therefore, the Gaussian filter parameters have little effect on the segmentation results.

In Table 1 and Table 2, the evaluation of segmentation results from 10 random data sets of PROMISE 12 are presented, which are indexed from a to j . Note that each set of data contains 32 images. It is noted that the numbers of MR images containing the prostate in each data set are not consistent, and we also list them in Table 1. Also, we also record the maximum, minimum, and average DSC (Table 1) and RVD (Table 2) values of each data set. The proposed method yields the average DSC of $89.21 \pm 1.82\%$. It indicates that the proposed method has reasonably high accuracy and robustness. The mean RVD is $-10.44 \pm 6.46\%$, which means that the proposed method tends to yield an over-segmentation result. However, the small RVD value indicates that over-segmentation is acceptable.

3.3 3D Model Reconstruction from a Contour Sequence

Figure 5 shows the segmented contour sequences and their corresponding 3D reconstruction for the models in Table 1. The reconstruction times for models a - j are 0.058s, 0.057s, 0.057s, 0.062s, 0.072s, 0.074s, 0.051s, 0.054s, 0.076s, 0.052s, respectively. For the 3D reconstruction of the prostate model, we simply triangulate the zone between each consecutive pair of contours, and make the first and last contours solid plates.

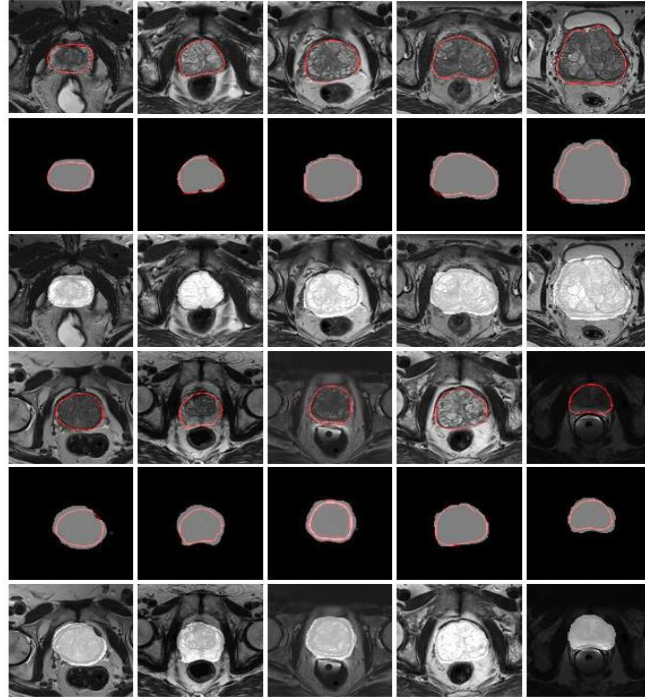


Figure 4: The images segmentation results of 10 random data sets from PROMISE 12.

	<i>Image set number</i>	<i>Number of images</i>	<i>Maximum DSC value</i>	<i>Minimum DSC value</i>	<i>Average DSC value</i>
<i>a</i>	Image 1	13	0.930769	0.789296	0.894687
<i>b</i>	Image 6	21	0.952865	0.767541	0.916436
<i>c</i>	Image 10	12	0.940283	0.748999	0.877896
<i>d</i>	Image 18	29	0.939687	0.779931	0.916799
<i>e</i>	Image 23	31	0.951122	0.745186	0.908472
<i>f</i>	Image 25	28	0.941955	0.754867	0.876209
<i>g</i>	Image 29	20	0.913971	0.765432	0.857853
<i>h</i>	Image 38	16	0.937323	0.776183	0.898916
<i>i</i>	Image 42	27	0.932042	0.765284	0.894847
<i>j</i>	Image 48	15	0.926923	0.757791	0.879006

Table 1: The DSC values of the segmentation results 10 random sets of PROMISE 12.

	<i>Image set number</i>	<i>Number of images</i>	<i>Minimum RVD value</i>	<i>Maximum RVD value</i>	<i>Average RVD value</i>
<i>a</i>	Image 1	13	-19.082278	4.301158	-11.362784

<i>b</i>	Image 6	21	-20.724637	6.681611	-13.624674
<i>c</i>	Image 10	12	-15.032081	8.212435	-7.553306
<i>d</i>	Image 18	29	-20.635673	7.883817	-16.473548
<i>e</i>	Image 23	31	-21.451483	11.15282	6.623682
<i>f</i>	Image 25	28	-23.968528	5.686636	-18.408493
<i>g</i>	Image 29	20	-17.516775	6.838488	-9.836724
<i>h</i>	Image 38	16	-17.624831	3.535004	-11.962915
<i>i</i>	Image 42	27	-16.806722	6.47925	-9.479252
<i>j</i>	Image 48	15	-20.493827	5.618812	-12.383417

Table 2: The RVD values of segmentation results of 10 random sets of PROMISE 12.

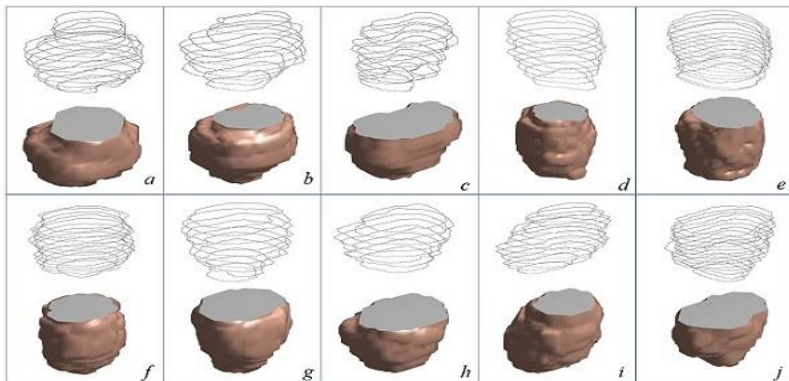


Figure 5: The results of 3D reconstruction of the models in Table 1.

3.4 Comparisons

For comparison purpose, we run our algorithm on a PC with Intel core i5-8250U CPU and 8 GB RAM. We compared the results of the proposed algorithm and other nine state-of-the-art prostate segmentation methods were chosen as the benchmark to evaluate our approach. Using PROMISE 12 dataset (10 data sets each of which contains 32 images), Table 3 shows the comparison results. Among the nine comparison methods, Klein [7] and Toth [55] put forward the very classic theories and models, although they did not use PROMISE 12 dataset, we also listed their results for comparison purpose. Note that the remaining 8 approaches used the same models for comparison. Milletari [15] achieved the minimum average segmentation time, but it costed 48 hours for preprocessing and the DSC is only 86.9 ± 3.3 . According to the scores listed in Table 3, the accuracy of our results is lower than those of Jia [41], Yu [55] and Tian [57], but we used significantly less time, and our algorithm is practical for implementation.

Refer to Table 3, Klein used the method based on Atlas Registration. Before each segmentation, the map was registered for about 15 minutes, and the average segmentation time took 900 seconds. Toth and Maan [57] used Active Shape Model and Active Appearance Model. In the process, the shape of the active model needs to be pre-defined, and the average segmentation time is about 150s and 100s, respectively. Qiu [58] and Tian used the active contour model, and the core and most time-consuming process of the algorithm are to construct complex energy equations. In other four methods, neural network is used to train the network for several hours before image segmentation. The preprocessing of our algorithm is to select a region of interest

(ROI) manually on the middle image of MR image sequence, this image will be taken as the first image of the sequence of MR images for the prostate. As discussed earlier, as the range of scan is chosen properly, this middle image is guaranteed to contain the target contour in its interior. By manual selection experiments, we find that this process can last for less than 10s since we may just roughly enclose a region.

To summarize, our approach achieved an excellent trade-off between accuracy and running time among the ten methods listed. In other words, faster segmentation algorithms either consumes more pre-processing time or leads to larger DSC. Those methods with higher calculation accuracy lag behind ours in running time, while those faster than ours cannot reach our calculation accuracy, i.e., our method can segment prostate MR images with acceptable accuracy in a short time. In addition, compared with the similar results achieved by Qian and Tian, our approach is relatively practical to implement for users.

<i>Paper</i>	<i>DSC(%)</i>	<i>Preprocessing time</i>	<i>Average segmentation time</i>	<i>Type</i>	<i>Data set</i>
Klein [7]	85-88	15min	900s	automatic	private
Toth [54]	87.66 ± 4.97	4.5min	150s	automatic	private
Milletari [15]	86.9 ± 3.3	48h	1s	automatic	PROMISE 12
Yu [55]	89.43	4h	12s	automatic	PROMISE 12
To [59]	89.01	5h	10s	automatic	PROMISE 12
Jia [41]	91 ± 3.6	40min	120s	semi-automatic	PROMISE 12
Tian [56]	89.3 ± 1.9	/	35s	semi-automatic	PROMISE 12
Maan [57]	81 ± 12	3h	100s	semi-automatic	PROMISE 12
Qiu [58]	88.5 ± 3.5	/	5s	semi-automatic	PROMISE 12
Ours	89.21±1.82	10s	3s	semi-automatic	PROMISE 12

Table 3: Comparison with other prostate MR segmentation algorithms.

4 CONCLUSION

In this paper, we propose an approach of identifying the contours of prostate features in a small set of MR images based on the prior information of the contour on the first image. Due to the small-scale (e.g., each of the experimental data set contains of 32 images), many advanced methods like neural network or unsupervised training processes involving machine learning cannot guarantee both accuracy and efficiency. The contour information on subsequent images is determined in a patch-by-patch manner. The patch is a sliding window whose center is the projection of a point on the prior information (i.e., an already computed contour). Our algorithm's significant advantage is that we merely focus on a local region of interest rather than the whole image when segmenting a medical image, which can effectively reduce the amount of computation in the image segmentation process and ignore noise and useless information in the other part of the image. We believe that the developed approach can be beneficial for fast male health examination in highly populated areas (e.g., China and India) whose hospitals are usually running out of their capacities.

In practice, medical images are noisy, and the target tissue pixels' intensities might be similar to those of other tissues. These affect the accuracy of the segmentation results. The developed approach will have more advantages for many images with complex and vague backgrounds since

we have a local focus. However, our method also has certain disadvantages since it depends on the accuracy of prior information. If the initial reference contour is not chosen correctly, it might lead to poor segmentation results. Therefore, our approach's success depends on the region of interest's choice to accurately cover the target tissue. Our proposed method requires the assumption that the prostate tissue is contained in the first chosen image, this requires the scan range to be as precise as possible. According to the manual selection experiments, the time for marking a coarse region of interest can usually be done in 10s, which is significantly less than existing training-learning based methods. Also, manual selection works well when the prostate boundary is vague, in which case automatic approaches usually fail.

In the future, detecting the region of interest in the first image when the prostate tissue is out of the usual position will be worthy of investigation. Also, the algorithms need to be improved further to reduce computational time while improving accuracy.

5 ACKNOWLEDGEMENT

This work was supported in part by the Science and Technology Commission of Shanghai Municipality Fund No. 18510745700.

Heng Zhang, <https://orcid.org/0000-0003-4317-4548>

Atul Thakur, <https://orcid.org/0000-0001-5937-4793>

Xiangzhi Wei, <https://orcid.org/0000-0002-4541-0017>

REFERENCES

- [1] Bray, F.; Ferlay, J.; Soerjomataram, I.; Siegel, R.; Torre, L.; Jemal, A.: Global cancer statistics 2018: GLOBOCAN estimates of incidence and mortality worldwide for 36 cancers in 185 countries, *CA Cancer J Clin* 68(6), 2018, 394–424. <https://doi.org/10.3322/caac.21492>
- [2] Ghose, S.; Oliver, A. et al.: A survey of prostate segmentation methodologies in ultrasound, magnetic resonance and computed tomography images, *Comput. Methods Programs Biomed*, 108, 2012, 262–287. <https://doi.org/10.1016/j.cmpb.2012.04.006>
- [3] Rohlfing, T.; Brandt, R.; Menzel, R.; Maurer, Jr, C. R.: Evaluation of atlas selection strategies for atlas-based image segmentation with application to confocal microscopy images of bee brains, *NeuroImage*, 21(4), 2004, 1428–1442. <https://doi.org/10.1016/j.neuroimage.2003.11.010>
- [4] Chandra, S.; Dowling, J.; Shen, K.: Patient specific prostate segmentation in 3-d magnetic resonance images, *IEEE Trans Med Imaging*, 31(10), 2012, 1955–1964. <https://doi.org/10.1109/TMI.2012.2211377>
- [5] Warfield, S.K.; Zou, K.H.; Wells, W.M.: Simultaneous truth and performance level estimation (STAPLE): an algorithm for the validation of image segmentation, *IEEE Trans Med Imaging*, 23(7), 2004, 903–921. <https://doi.org/10.1109/TMI.2004.828354>
- [6] Langerak.; Robin, T.; Heide, V. et al.: Label fusion in atlas-based segmentation using a selective and iterative method for performance level estimation (SIMPLE), *IEEE Trans Med Imaging*, 29(12), 2010, 2000–2008, <https://doi.org/10.1109/TMI.2010.2057442>
- [7] Klein, S.; van der Heide, U.; Lips, I.; van Vulpen, M.; Staring, M.; Pluim, J.: Automatic segmentation of the prostate in 3D MR images by atlas matching using localized mutual information. *Med Phys*, 35(4), 2008, 1407–1417. <https://doi.org/10.1118/1.2842076>
- [8] Yang, X.; Jani, A.B.; Rossi, P.J.; Hui, M.; Curran, W.; Tian, L.: Patch-Based Label Fusion for Automatic Multi-Atlas-Based Prostate Segmentation in MR Images, *Proc SPIE Int Soc Opt Eng*, 9786, 2016, 978621. <https://doi.org/10.1117/12.2216424>
- [9] Dura, E.; Domingo, J.; Göçeri, E.; Martí-Bonmatí, L.: A method for liver segmentation in perfusion MR images using probabilistic atlases and viscous reconstruction, *Pattern Analysis and Applications* 21(4), 2017, 1083–1095. <https://doi.org/10.1007/s10044-017-0666-z>

- [10] Jia, D.; Wei, D.; Socher, R.; Li, L.; Kai, L.; Li, F.: ImageNet: A large-scale hierarchical image database, IEEE Conference on Computer Vision and Pattern Recognition, 2009, 248-255.
- [11] Krizhevsky, A.; Sutskever, I.; Hinton, G.E.: ImageNet classification with deep convolutional neural networks, Communications of the ACM, 60(6), 2017, 84-90. <https://doi.org/10.1145/3065386>
- [12] Simonyan, K.; Zisserman, A.: Very deep convolutional networks for large-scale image recognition, conference paper at ICLR, 2015. <https://arxiv.org/abs/1409.1556>
- [13] Szegedy, C.; Wei, L.; Jia, Y.; Sermanet, P.; Rabinovich, A.: Going deeper with convolutions, IEEE Computer Society, 2014. <https://doi.org/10.1109/CVPR.2015.7298594>
- [14] Ronneberger, Q.; Fischer, P.; Brox, T.: U-net: Convolutional networks for biomedical image segmentation, Springer, Cham, 2015. <https://doi.org/10.1007/978-3-662-54345-03>
- [15] Milletari, F.; Navab, N.; Ahmadi, S-A.: V-Net: Fully convolutional neural networks for volumetric medical image segmentation, 2016 Fourth International Conference on 3D Vision (3DV), Stanford, CA, 2016, 565-571. <https://doi.org/10.1109/3DV.2016.79>
- [16] Girshick, R.: Fast R-CNN, Computer Science, 2015. <https://doi.org/10.1109/ICCV.2015.169>
- [17] Chen, H.; Qi, X.; Yu, L.; Heng, P.-A.: DCAN: Deep contour aware networks for accurate gland segmentation, Med Image Anal, 36, 2017, 135-146. <https://doi.org/10.1016/j.media.2016.11.004>
- [18] Creswell, A.; White, T. et al: Generative Adversarial Networks: An Overview, IEEE Signal Processing Magazine, 35(1), 2018, 53-65. <https://doi.org/10.1109/MSP.2017.2765202>
- [19] Zhu, Q.; Du, B.; Turkbey, B.; Choyke, P.L.; Yan, P.: Deeply-supervised CNN for prostate segmentation, Neural Networks (IJCNN), 2017 International Joint Conference, 2017, 178-184. <https://doi.org/10.1109/IJCNN.2017.7965852>
- [20] Isensee, F.; Petersen, J.; Kohl, S.; Jäger, P.; Maier-Hein, K.H.: nnU-Net: Breaking the Spell on Successful Medical Image Segmentation, arXiv:1904.08128, 2019.
- [21] Cheng, R.; Roth, H. R.; Lu, L.; Wang, S.; Turkbey, B.; Gandler, W.; McCreedy, E. S.; Agarwal, H. K.; Choyke, P.; Summers, R. M.; McAuliffe, M.J.: Active appearance model and deep learning for more accurate prostate segmentation on MRI, Medical Imaging. Vol. 9784 of Proceedings of the SPIE, 2016, 9784. <https://doi.org/10.1117/12.2216286>
- [22] Kass, M.; Witkin, A.; Terzopoulos, D.: Snakes: Active contour models, Int. J. Comput. Vis., 1, 1988, 321-331. <https://doi.org/10.1007/BF00133570>
- [23] Ji, Z.; Xia, Y.; Sun, Q.; Cao, G.; Chen, Q.: Active contours driven by local likelihood image fitting energy for image segmentation, Information Sciences, 301, 2015, 285-304. <https://doi.org/10.1016/j.ins.2015.01.006>
- [24] Li, C.; Xu, C.; Gui, C.; Fox, M.: Distance regularized level set evolution and its application to image segmentation, IEEE Trans. Image Process, 19 (12), 2010, 3243-3254. <https://doi.org/10.1109/TIP.2010.2069690>
- [25] Yuan, J.J.; Wang, J.J.: Active contours driven by local intensity and local gradient fitting energies, Int. J. Pattern Recognit. Artif. Intell, 28(03), 2014, 1455006. <https://doi.org/10.1142/S0218001414550064>
- [26] Lankton, S.; Tannenbaum, A.: Localizing region-based active contours, IEEE Trans. Image Process. 17 (11), 2008, 2029-2039. <https://doi.org/10.1109/TIP.2008.2004611>
- [27] Thomas, K.; David, B.; Guido, B.: Snake-based segmentation of teeth from virtual dental casts, Computer-Aided Design and Applications, 7(2), 2010, 221-233. <https://doi.org/10.3722/cadaps.2010.221-233>
- [28] Li, C.; Kao, C.; Gore, J.; Ding, Z.: Minimization of region-scalable fitting energy for image segmentation, IEEE Trans. Image Process. 17 (10), 2008, 1940-1949. <https://doi.org/10.1109/TIP.2008.2002304>
- [29] Jiang, X.; Li, B.; Yuan, J.; Wu, X.: Active Contour Driven by Local Gaussian Distribution Fitting and Local Signed Difference Based on Local Entropy, International Journal of Pattern Recognition and Artificial Intelligence, 2016, 30(3). <https://doi.org/10.1142/S0218001416550119>

- [30] Yang, Y.; Zhao, Y.; Wu, B.: Efficient active contour model for multiphase segmentation with application to brain MR images, *International Journal of Pattern Recognition & Artificial Intelligence*, 2013, 27(1), 1355001. <https://doi.org/10.1142/S021800141355001X>
- [31] Wang, H.; Liu, M.: A novel active contour model for image segmentation and bias correction using guided image filtering regularization term, *International Journal of Pattern Recognition and Artificial Intelligence*, 2017, 31(07), 1754013. <https://doi.org/10.1142/S0218001417540131>
- [32] Artan, Y.; Haider, M. A.; Yetik, I.S.: Graph-based active contours using shape priors for prostate segmentation with MRI, *IEEE International Symposium on Biomedical Imaging (ISBI): From Nano to Macro*, 2011, 1459–1462. <https://doi.org/10.1109/ISBI.2011.5872675>
- [33] Miao, J. Huang, T.; Zhou, X.; Wang, Y.; Liu, J.: Image segmentation based on an active contour model of partial image restoration with local cosine fitting energy, *Information Sciences*, 2018, 447:52-71. <https://doi.org/10.1016/j.ins.2018.02.007>
- [34] Mabood, L.; Ali, H.; Badshah, N.; Chen, K.; Khan, G.A.: Active contours textural and inhomogeneous object extraction, *Pattern Recognition*, 55, 2016, 87-99. <https://doi.org/10.1016/j.patcog.2016.01.021>
- [35] Pratondo, A.; Chui, C.; Ong, S.: Integrating machine learning with region-based active contour models in medical image segmentation, *Journal of Visual Communication and Image Representation*, 43, 2017, 1-9. <https://doi.org/10.1016/j.jvcir.2016.11.019>
- [36] Pien, H.; Desai, M.; Shah, J.: Segmentation of MR images using curve evolution and prior information, *International Journal of Pattern Recognition & Artificial Intelligence*, 1997, 11(8), 1233-1245. <https://doi.org/10.1142/S0218001497000573>
- [37] Yan, P.; Xu, S.; Turkbey, B.; Kruecker, J.: Discrete deformable model guided by partial active shape model for TRUS image segmentation, *IEEE Trans Biomed Eng*, 57(5), 2010, 1158-1166. <https://doi.org/10.1109/TBME.2009.2037491>
- [38] Vikal, S.; Haker, S.; Tempany, C.; Fichtinger, G.: Prostate contouring in MRI guided biopsy, *Proceedings of SPIE - The International Society for Optical Engineering*, 7259, 72594A.
- [39] Andrade, S.; Skeika, E.; Aires, S.: Segmentation of the Prostate Gland in Images Using Prior Knowledge and Level Set Method, *2017 Workshop of Computer Vision*, 2017, 31-36.
- [40] Yang, X.; Zhan, S.; Xie, D.; Zhao, H.; Kurihara, T.: Hierarchical prostate MRI segmentation via level set clustering with shape prior, *Neurocomputing*, 257, 2017, 154-163. <https://doi.org/10.1016/j.neucom.2016.12.071>
- [41] Jia, H.; Xia, Y.; Song, Y.; Cai, W.; Fulham, M.; Feng, D.: Atlas registration and ensemble deep convolutional neural network-based prostate segmentation using magnetic resonance imaging, *Neurocomputing*, 275, 2018, 1358-1369. <https://doi.org/10.1016/j.neucom.2017.09.084>
- [42] Canny, J.: A Computational Approach to Edge Detection, *IEEE Transactions on Pattern Analysis and Machine Intelligence*, 1986, PAMI-8(6), 679-698. <https://doi.org/10.1109/TPAMI.1986.4767851>
- [43] Litjens, G.; Debats, O.; Barentsz, J.; Karssemeijer, N.; Huisman, H.: Computer-aided detection of prostate cancer in MRI, *IEEE Transactions on Medical Imaging*, 33(5), 2018, 1083-1092. <https://doi.org/10.1109/TMI.2014.2303821>
- [44] Gonzalez, R. C.; Woods, R. E.: *Digital image processing*. Prentice Hall International, 2008, 28(4):484 - 486. <https://doi.org/10.1109/TASSP.1980.1163437>
- [45] Rabby, M.; Chowdhury, B.; Kim, J.H.: A Modified Canny Edge Detection Algorithm for Fruit Detection & Classification, *2018 10th International Conference on Electrical and Computer Engineering (ICECE)*. 2018.
- [46] Kaur, B.; Garg, A.: Mathematical morphological edge detection for remote sensing images. *IEEE*, 2011. <https://doi.org/10.1109/ICECTECH.2011.5942012>
- [47] Kabade, A. L.; Year, I.; Tech, M.: Canny edge detection algorithm.
- [48] Stosic, Z.; Rutesic, P.: An Improved Canny Edge Detection Algorithm for Detecting Brain Tumors in MRI Images. In *International Journal of Signal Processing (Vol. 03)*. International Association of Research and Science.

- [49] Jia, Y.D.: "Machine Vision," Beijing: Science Press, 2000, pp.97–100 Rong,
- [50] W.B.; Li, Z.J.; Wei Zhang, W.; Sun, L.N.: An Improved Canny Edge Detection Algorithm. 2014 IEEE International Conference on Mechatronics and Automation
- [51] Litjens, G.; Toth, R. et al: Evaluation of prostate segmentation algorithms for MRI: The PROMISE12 challenge, Medical Image Analysis, 2014, 18(2), 359-373. <https://doi.org/10.1016/j.media.2013.12.002>
- [52] Tian, Z.; Liu, L.; Zhang, Z.; Fei, B.: Superpixel-Based Segmentation for 3D Prostate MR Images, IEEE Transactions on Medical Imaging, 35(3), 2016, 791-801. <https://doi.org/10.1109/TMI.2015.2496296>
- [53] Heimann, T.; van Ginneken, B.; Styner, M.: Comparison and evaluation of methods for liver segmentation from CT datasets, IEEE Trans. Med. Imaging, 28, 2009, 1251–1265. <https://doi.org/10.1109/TMI.2009.2013851>
- [54] Toth, R.; Madabhushi, A.: Multi-feature landmark-free active appearance models: application to prostate MRI segmentation, IEEE Transactions on Medical Imaging, 31(8), 2012, 1638-1650. <https://doi.org/10.1109/TMI.2012.2201498>
- [55] Yu, L.; Yang, X.; Hao, C.: Volumetric ConvNets with Mixed Residual Connections for Automated Prostate Segmentation from 3D MR Images, AAAI, 2017, 66-72.
- [56] Tian, Z.; Liu, L.; Zhang, Z.; Xue, J.; Fei, B.: A supervoxel-based segmentation method for prostate MR images. Medical Physics. vol. 44(2), 2017, 558-569. <https://doi.org/10.1002/mp.12048>
- [57] Maan, B.; Heijden, F.: Prostate MR image segmentation using 3D Active Appearance Models, Grand Challenges in Medical Image Analysis, PROMISE12, 2012, 44-51.
- [58] Qiu, W.; Yuan, J.; Sun, Y.: Prostate Segmentation: An Efficient Convex Optimization Approach with Axial Symmetry Using 3D TRUS and MR Images, IEEE Transactions on Medical Imaging, 2013, 0278-0062.
- [59] To, M.: Deep dense multi-path neural network for prostate segmentation in magnetic resonance imaging, International Journal of Computer Assisted Radiology and Surgery, 13, 2018, 13, 1687–1696. <https://doi.org/10.1007/s11548-018-1841-4>

APPENDIX

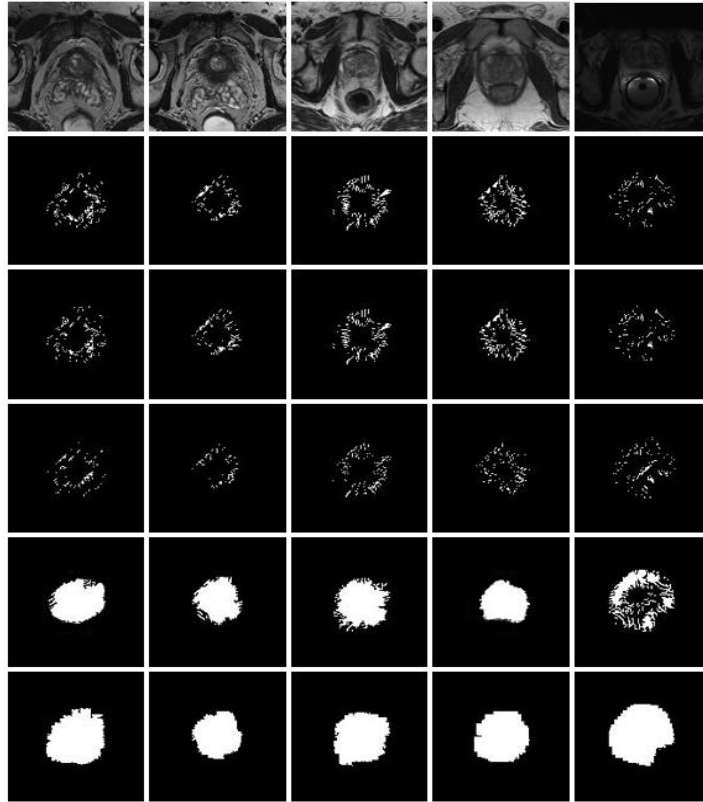


Figure 6: The Segmentation results of different operators used in proposed algorithm. From top to bottom are the original images, the results of Sobel operator, Prewitt operator, Roberts operator, Canny operator, and Fuzzy Logical operator, respectively.

Refer to Figure 6 and Table 4, in terms of segmentation results, Canny operator is superior to the first-order derivative operators like Sobel operator, Prewitt operator and Roberts operator, but it is inferior to the Fuzzy Logical operator. And Canny operator is significantly superior to Fuzzy Logical operator in terms of efficiency (~ 10 times). Therefore, Canny operator is exploited as an edge segmentation tool for the medical images with noise and indistinct edge information.

	Sobel	Prewitt	Roberts	Canny	Fuzzy Logical
Image1	0.320949	0.284765	0.277686	0.291681	3.040971
Image2	0.255813	0.231197	0.271382	0.282608	2.264425
Image3	0.298008	0.243339	0.256423	0.306242	2.919713
Image4	0.248287	0.242393	0.312632	0.309851	3.931292
Image5	0.290793	0.281304	0.263489	0.256831	2.489202

Table 4: The segmentation time of different operators in the proposed algorithm.